The Superswell and Mantle Dynamics Beneath the South Pacific

MARCIA K. MCNUTT AND ANNE V. JUDGE

The region of sea floor beneath French Polynesia (the "Superswell") is anomalous in that its depth is too shallow, flexural strength too weak, seismic velocity too slow, and geoid anomaly too negative for its lithospheric age as determined from magnetic isochrons. These features evidently are the effect of excess heat and extremely low viscosity in the upper mantle that maintain a thin lithospheric plate so easily penetrated by volcanism that 30 percent of the heat flux from all hot spots is liberated in this region, which constitutes only 3 percent of the earth's surface. The low-viscosity zone may facilitate rapid plate motion and the development of small-scale convection. A possible heat supply for the Superswell is a mantle reservoir enriched in radioactive isotopes as suggested by the geochemical signature of lavas from Superswell volcanoes.

THE SEA FLOOR BENEATH FRENCH POLYNESIA IN THE South Pacific is unusual as compared to oceanic lithosphere elsewhere in almost all respects. As the lithosphere increases in age from 0 million years ago (Ma) at the East Pacific Rise (Fig. 1) to more than 80 Ma in the west, it subsides more slowly than at the rate predicted by the 125-km-thick plate model, which provides a good fit to bathymetry and heat flow data in the North Pacific, Atlantic, and Indian oceans (*1*). McNutt and Fischer (*2*) termed this region the "Superswell" in recognition of 250- to 1000-m depth anomalies covering an area of approximately 18 million square kilometers and proposed that the region is underlain by a lithospheric plate only 70 km thick. Although the idea of a thinner thermal plate can account quantitatively for the anomalous sea-floor depths and qualitatively for the low velocities of seismic surface waves (*3*), the weak elastic strength of the lithosphere (*4, 5*), and its high vulnerability to midplate (hot spot) volcanism, in a number of respects this model is incomplete. For example, it provides no insight into why volcanic eruptions on the Superswell are characterized by an unusual geochemical signature derived from a source rich in radioactive elements such as rubidium compared to normal oceanic upper mantle (*6*), why both spreading rate and absolute velocity of the plate with respect to the mantle reach the highest values on the earth in the region of the Superswell (7), or why superswell-type features appear to be an intermittent feature of this part of the world for at least the 100 past million years (*8, 9*).

More importantly, the model completely fails to explain why the geoid anomaly, which measures variations in the height of the earth's sea-level equipotential surface caused by subsurface mass anomalies, is strongly negative (Fig. 2) over the Superswell. The amplitude of a geoid signal decreases as the inverse of distance between sea level and the location of an anomalous mass. For uplifted sea floor compensated by an equal but opposite mass deficit caused by thermally expanded rock located in the lower lithosphere, the geoid high from the shallow mass excess is larger than the geoid low from its deeper compensation, leading to a small net geoid high. Thus the large geoid low over the Superswell cannot be related to a thinned lithosphere and can only be understood in terms of the mass anomalies driving convection in the mantle and the deformations they induce on surface and subsurface density interfaces. The goal of this study is to combine all of the available geophysical and geological information to understand the properties of the convecting mantle and how it interacts with the lithosphere beneath the Superswell to produce 30 percent of the global mass and heat flux from all hot spots (*10*) concentrated in a region that covers only 3 percent of the earth.

M. K. McNutt and A. V. Judge are in the Department of Earth, Atmospheric, and Planetary Sciences, Massachusetts Institute of Technology, Cambridge, MA 02139.

Approach to Data Analysis

Although the long-wavelength geoid anomaly over French Polynesia indicates the importance of convectively maintained thermal anomalies in the mantle in producing the Superswell, the geoid data alone do not uniquely determine their magnitude and location. For example, all of the following perturbations to a standard oceanic crust and mantle model could lead to a geoid anomaly of 1 m at the earth's surface: thickening the crust from 6 to 11 km; reheating the lithosphere by 250°C between depths of 80 and 90 km; warming a uniform viscosity mantle by 10°C between depths of 300 and 400 km; and cooling the mantle by 60°C between depths of 300 and 400 km within a shallow low-viscosity zone. Although the geoid alone would not distinguish these models, they all do differ in the amount of surface uplift predicted: 1 km, 100 m, 40 m, and −140 m for the four anomalous thermal structures, respectively. Given our ignorance of the viscosity structure of the mantle beneath the Superswell, by isolating that component of the anomalous depth and geoid arising from mantle convection from the lithospheric contribution we can estimate both the mantle viscosity and the temperature structure.

The approach we take is first to use the surface-wave velocity anomalies, short-wavelength geoid anomalies over individual hot-spot chains on the Superswell, and estimates of the thickness of the elastic plate supporting the hot-spot volcanoes, all of which are primarily sensitive to the thermal structure in the lithosphere, to constrain the lithospheric component of the thermal anomaly. We then remove the predicted effects of the thermal anomalies within

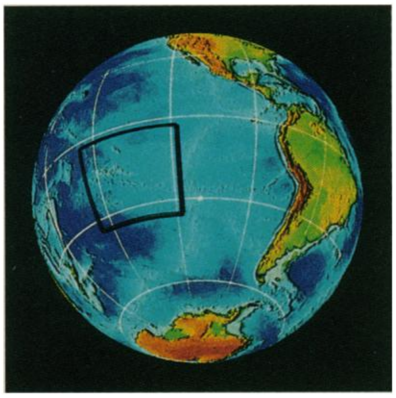

Fig. 1. Hemispheric projection of bathymetry of the South Pacific (*27*). The Superswell is the area of shallow sea floor inside the black box containing the volcanic chains of French Polynesia. The East Pacific Rise is the long, continuous ridge along the eastern boundary of the Superswell. [Adapted from National Oceanic and Atmospheric Administration map MGG-2]

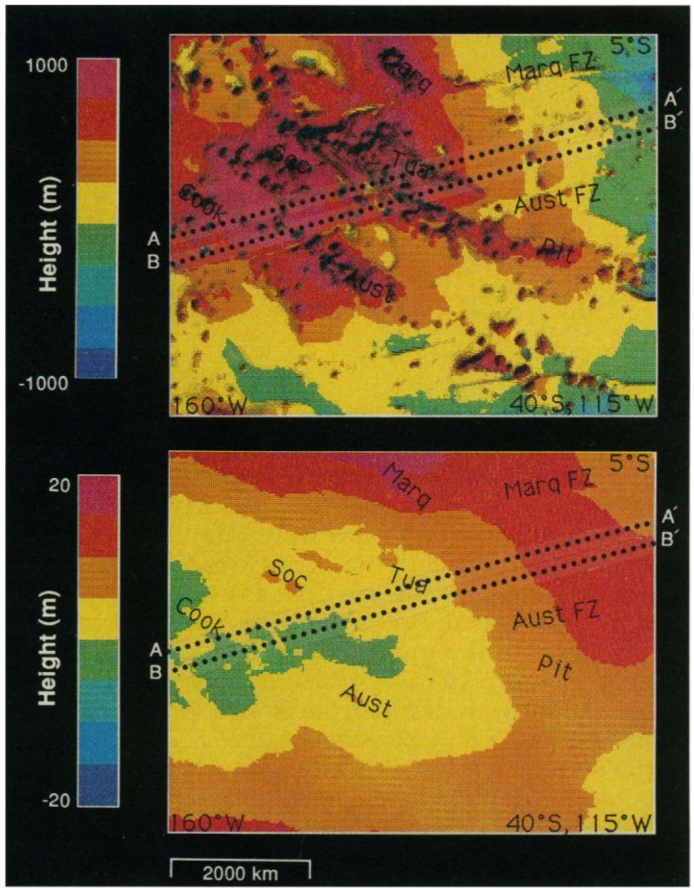

Fig. 2. Depth (**top**) and geoid (**bottom**) anomalies over the Superswell for the area outlined in Fig. 1. One obtains the depth anomalies by subtracting from the observed bathymetry (*27*) the depth predicted for a standard 125-km-thick thermal plate (*1*) as a function of lithospheric age (*2*). For the geoid data (*28*), we removed a reference geoid (GEM9) to degree and order 4 before correcting for lithospheric age. Prominent tectonic features in the area are the Marquesas, Society, Tuamotu, Cook, Austral, and Pitcairn island chains and the Marquesas and Austral fracture zones. The dotted lines show the locations of the two profiles in Fig. 6.

the lithosphere from the bathymetric and geoid observations in order to model what remains in terms of dynamic flow in the mantle. In the lithosphere, all geophysical observations and thermal anomalies are referenced with respect to the 125-km-thick plate model (*1*). In the asthenosphere, temperature is referenced to an adiabat. Geophysical anomalies are assumed to arise solely from variations in temperature, rather than from major element composition or mineralogy, relative to the standard model. In the end, the internal consistency of our results from modeling several different sorts of data justifies ignoring nonthermal sources for the depth, geoid, and seismic velocity anomalies.

The Lithospheric Component of the Superswell

Regional lithospheric thinning as constrained by seismic surface waves. Love waves are horizontally polarized shear waves propagating through a surface layer and thus are extremely sensitive to shallow variations in the shear wave velocity β, which depends on rock density and its temperature-sensitive shear modulus. Nishimura and Forsyth (*3*) demonstrated that the lateral distribution of Love-wave phase velocities across the Pacific for periods of 40, 67, 91, and 125 s is correlated with lithospheric age (Fig. 3) and therefore presumably is caused by cooling of the oceanic lithosphere. Before we could use anomalies in Love-wave phase velocity with respect to this standard age-dependent Pacific model to investigate thermal anomalies beneath the Superswell, it was necessary to confirm quantitatively the hypothesis that Love-wave velocity primarily reflects lithospheric thermal structure and to calibrate the change in seismic velocity with temperature as required by the Love-wave data. The theoretical phase velocity C_n for waves of period n at time t depends on the temperature of the lithosphere $T(t,z)$ given by the standard 125-km-thick plate model (*1*) via (*11*)

$$C_n(t) = C_n(125) - \frac{\partial\beta}{\partial T}\int_0^{125\text{ km}} \frac{\partial C_n}{\partial\beta}(z)[T(t,z) - T(125,z)]dz \quad (1)$$

in which $\partial C_n/\partial\beta\ (z)$ is the Love-wave "kernel" (*12*) for period n that describes the relation between changes in the phase velocity and changes in the shear wave velocity as a function of depth z based on a standard earth model (Fig. 4). The quantities $C_n(125)$ and $T(125,z)$ are phase velocities and temperatures for 125-Ma lithosphere, respectively. The change in shear wave velocity with temperature $\partial\beta/\partial T$, as determined by a least-squares fit to the observations (Fig. 3), is -0.618 ± 0.108 m s^{-1} °C^{-1}, which is consistent with the change in *P*-wave velocity with temperature $\partial\alpha/\partial T = -0.5$ m s^{-1} °C^{-1} found from modeling wave propagation along subducting slabs (*13*) if we assume that $1.1 \times \partial\alpha/\partial T = \partial\beta/\partial T$ (*14*). The only major misfit occurs at the youngest lithospheric ages where velocities are slower than predicted by the thermal model at all periods. This reduction in seismic velocity on oceanic crust less than 7 Ma is also observed in near-bottom seismic refraction data and is caused by age-related modifications to the physical properties of the uppermost crust, such as modifications to crack geometry and reduction in porosity by alteration and precipitation (*15*). Thus we conclude that the standard thermal plate model provides a good explanation for the observed age-dependent changes in phase velocities averaged over the entire Pacific for lithosphere older than 10 Ma and that the effective value for $\partial\beta/\partial T$ over lithospheric-length scales is well constrained by this analysis to lie between -0.5 and -0.7 m s^{-1} °C^{-1}.

After removal of this empirical velocity-age effect caused by cooling of normal oceanic lithosphere (Fig. 3), the residual velocities over the Superswell are slow (Fig. 5), presumably reflecting hotter temperatures beneath the Superswell than for normal lithosphere (*16*). Because the anomaly is largest for the 40-s waves and decreases with increasing period, no model involving thermal anomalies confined to depths below a 125-km-thick lithosphere is capable of fitting the phase velocity anomalies as a function of period. Rather, the thermal anomalies must be concentrated in the depth range 50 to 100 km where the kernel in Fig. 4 for 40-s waves lies the greatest distance above the kernels for the longer periods; this relation requires substantial reheating of the lithosphere. We estimated the amount of lithospheric thinning needed to produce the theoretical Love-wave anomalies ΔC_n (Fig. 5) using

$$\Delta C_n(t) = \frac{\partial \beta}{\partial T} \int_0^{125 \text{ km}} \frac{\partial C_n}{\partial \beta}(z)[T_{\text{thin}}(z) - T_{125}(z)]dz \qquad (2)$$

in which $[T_{\text{thin}}(z) - T_{125}(z)]$ is the temperature difference as a function of depth between a standard thermal plate that is 125 km thick and a thinned lithosphere. The best match to the amplitude of the observed velocity anomalies as a function of period (Fig. 5) is attained for lithosphere 60 to 80 million years old thinned to depths of 60 to 75 km, with $\partial\beta/\partial T$ equal to -0.5 to -0.7 m s^{-1} °C^{-1}. The data cannot be matched with a lithosphere thicker than 75 km beneath the Superswell, even if we assume a more negative value for $\partial\beta/\partial T$, because the temperature differences would not be concentrated at shallow enough depth to produce the required reduction in velocity anomaly with increasing period.

The thermal anomalies in the thinned lithosphere beneath the Superswell that produce the slow Love waves reach 300°C. Temperature anomalies below 125 km may also exist, but the fact that the 67-, 91-, and 125-s anomalies are smaller than the anomaly at 40 s requires that any thermal anomalies below 150 km must be much smaller in magnitude than 300°C.

On the basis of modeling the Love-wave data, we conclude that the lithosphere has been thinned beneath the Superswell. The depth and geoid observations are hereafter referenced with respect to a 75-km-thick lithosphere, because that is the thickest plate consistent with the velocity anomalies. Although the depth of the sea floor was not used as a constraint in determining the lithospheric thickness beneath the Superswell, the predicted rate of subsidence of a 75-km-thick plate also accounts for most of the depth anomaly over the Superswell (Fig. 6), except on young lithosphere near the East Pacific Rise and in the immediate vicinity of seamount chains. This model does not, however, explain any part of the geoid signal and in fact amplifies the geoid low over the Superswell relative to the values to the east, north, and south.

Local lithospheric thinning beneath hot spot swells. Before interpreting the remaining depth and geoid anomalies in terms of mantle flow, the effect of individual volcanic chains superimposed on the Superswell must be removed from the data. Volcanoes on the Superswell lie along a series of northwest-trending lineations formed as the Pacific plate drifted over several relatively fixed hot spots (Marquesas, Society, Austral, and Pitcairn) that now lie beneath the youngest, southeast ends of the island chains (Fig. 1). The Tuamotu Plateau is the oldest of the volcanic features, having been formed by a hot spot situated on or near the mid-ocean ridge during the Late Cretaceous–Early Tertiary (45 to 30 Ma). The other hot spot chains formed off-ridge during the past 25 million years, and their younger volcanoes presently lie on 500- to 1000-km-wide swells of broadly uplifted sea floor that taper down to the northwest. Such swells are found surrounding all young hot spots and are a regional thermal effect of hot spot volcanism.

Correction of the depth and geoid data for the effects of hot spot volcanism is straightforward in the case of the Tuamotu Plateau because the steep slopes of the plateau allow its bathymetric signature to be distinguished from the surrounding sea floor, and the corresponding theoretical geoid is easily calculated with the assumption of local compensation by thickened crust (*17*). Removal of the midplate swells is not as straightforward because their slopes merge smoothly into those of neighboring swells and the surrounding sea floor. Rather than estimate the swell depth and geoid anomalies "by eye," we predicted the depth anomaly and corresponding geoid anomaly for the midplate swells by computing estimates of the depth z_ℓ (*18*) and planform (*19*) of the thermal load beneath the swell and the parameters describing the compensation of the surface load (Table 1). This approach is somewhat circular in that the geoid and depth data themselves are used to determine the parameters in the model, but it has the advantages that the predicted geoid and swell both arise from the same model that has a physical basis (*20*), and, given the same model parameters (Table 1), the result can be reproduced.

Table 1. Parameters used to model midplate swells. T_e is the elastic plate thickness, ρ_c is the density of volcanic rock, z_t is the observed depth to the topographic load, z_m is the observed depth to the Moho, and z_ℓ is the observed depth to the thermal load beneath the swell. Both z_m and ρ_c are typical for oceanic areas, and z_t is directly observed. We estimate the uncertainties in T_e and z_ℓ to be ±3 km and ±5 km, respectively, using the method of McNutt and Shure (*18*).

Swell	T_e (km)	ρ_c (kg m^{-3})	z_t (km)	z_m (km)	z_ℓ (km)
Marquesas	19	2700	6	11	45
Society	20	2700	5	13	43
Austral	8	2700	5	13	42
Pitcairn	0	2700	4.5	13	13*

*Crustal compensation.

Except for the Marquesas swell, which lies on apparently normal lithosphere north of the Marquesas Fracture Zone (*2*), both the elastic plate thickness T_e and the compensation depth z_ℓ for these swells are much less than the values typical for swells built on normal oceanic lithosphere (*21*). Because T_e and z_ℓ are two independent measures of how shallow heat from the spot has penetrated into the plate, this result suggests that the excess heat from hot spots on the Superswell resides at shallow depths in the lithosphere, even though geochemical evidence suggests that, relative to the Hawaiian hot spot, the weak Polynesian hot spots did not melt large volumes of lithosphere (*22*). One way to reconcile the geophysical evidence for shallow heat beneath the hot spot volcanoes without violating the geochemical evidence for little melting of the lithosphere by the hot

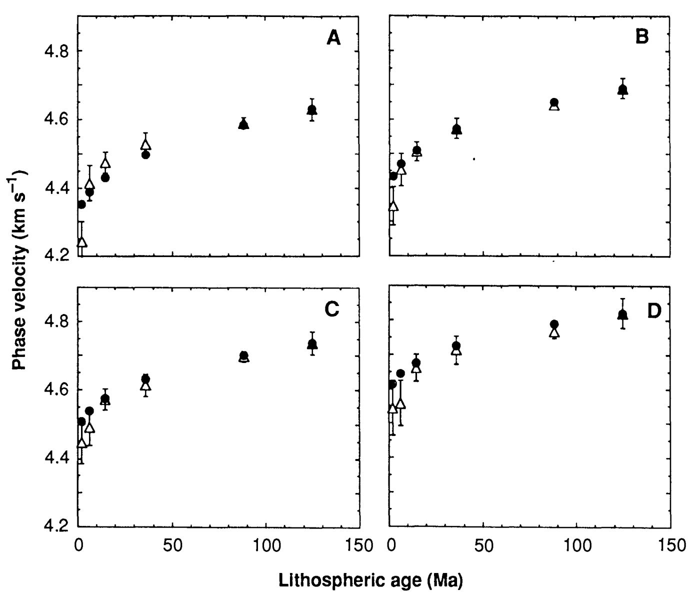

Fig. 3. Open triangles show the observed Love-wave phase velocities for (**A**) 40-, (**B**) 67-, (**C**) 91-, and (**D**) 125-s surface waves as a function of increasing age of the oceanic lithosphere (*3*). The 2σ errors are 95 percent confidence intervals for 115 Love-wave paths crossing the Pacific (*3*). Closed circles show the predicted phase velocity on the assumption that the decrease from the value for 125-Ma lithosphere with decreasing age for each period is caused solely by the hotter temperatures at younger ages in a 125-km-thick thermal plate with $\partial\beta/\partial T = -0.618$ m s^{-1} °C^{-1}.

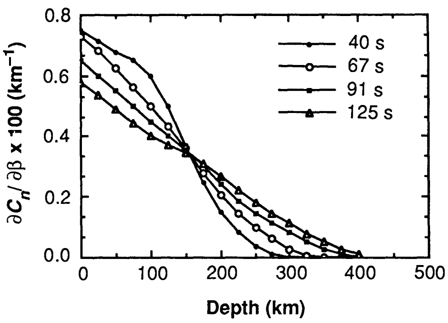

Fig. 4. Kernels relating phase velocity C_n to shear wave velocity β as a function of depth for four different periods of Love waves based on the model of Dziewonski *et al.* (*29*).

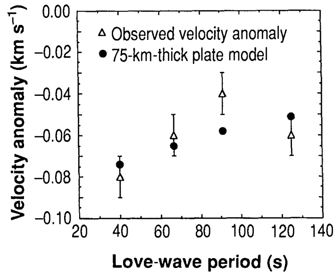

Fig. 5. Love-wave slowness anomalies at the center of the Superswell for 40-, 67-, 91-, and 125-s surface waves (*8*). Only the peak values (referenced with respect to the empirical increase in velocity with increasing lithospheric age in Fig. 3) are plotted; the observed anomalies taper to zero along the edge of the Superswell. Error bars (2σ) assigned to data were formally determined only for the 67-s waves (*3*). Predicted slowness anomalies are calculated from the difference in temperature at 80 Ma between lithosphere 75 km thick and 125 km thick.

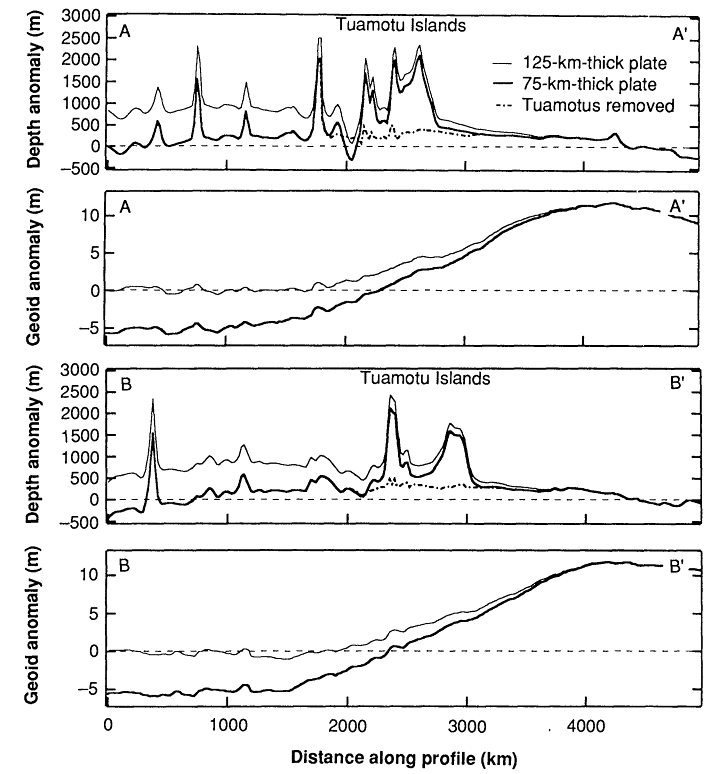

Fig. 6. Comparison of profiles of depth and geoid anomalies over the Superswell referenced to plates 125 km and 75 km thick at the locations marked by the dotted lines in Fig. 2.

spot is to assume that the lithospheric plate was regionally thinned before it encountered the hot spots, in agreement with the evidence from Love waves for a 75-km-thick plate. This result suggests that the hot spots are not the cause of the thin lithosphere.

The residual depth anomalies referenced to the 75-km-thick plate and stripped of the hot spot swells (Fig. 7) are no longer correlated with age, as in Fig. 2, or with the location of volcanic chains. The corresponding corrections applied to the geoid anomalies (Fig. 7), which are relatively insensitive to lithospheric structure, have not changed their pattern but have only increased their amplitude. The bathymetric high, now centered over the Superswell, is still correlated with a "saddle" in the geoid, as it was in Fig. 2, but the lithospheric corrections have reduced the magnitude of the topographic signal, which cannot be accounted for by the thermal structure of the lithosphere, from more than 1 km to less than 250 m. This result is not sensitive to the parameters used from Table 1 to within their uncertainties. The signature of individual volcanoes still remains in these maps, but their signal is of short enough wavelength that it does not interfere with modeling the dynamic component to the Superswell.

The Dynamic Component of the Superswell

The pattern of depth and geoid anomalies shown in Fig. 7 contains information on the viscosity structure of and thermal anomalies in the mantle, although it cannot constrain a unique structure of convection. A complete analysis of this problem requires that these depth and geoid maps be compared to those predicted by convectively maintained thermal anomalies in a fluid with heat sources, boundary conditions, and rheology appropriate to the mantle (none of which is known in detail). Ratios of geoid anomaly to depth anomaly as a function of wavelength (admittance estimates) can be used, however, to place some broad constraints on the viscosity structure of the mantle that is consistent with these data (Fig. 8).

At wavelengths of 5000 km (for example, an east-west transect across the Superswell), there is a weak positive correlation between geoid and depth anomalies, whereas at intermediate wavelengths of 2500 km (for example, a north-south transect across the Superswell), the correlation is strongly negative. This admittance pattern is a robust feature of the Superswell in that it is insensitive to how the wave number bands are selected for azimuthal averaging, whether the effects of midplate swells are accounted for (which have greater effect on the admittance at wavelengths less than 2000 km), and modest changes in the lithospheric plate thickness chosen as the reference.

The amplitude of the depth and geoid anomalies over the Superswell and their ratio as a function of wavelength can be compared to predicted dynamic topography, geoid, and admittance for various viscosity models. The thermal anomalies $\Delta T_{\ell,m}$ at depth are related to the predicted dynamic topography $h_{\ell,m}$ for spherical harmonic degree and order ℓ, m via an integral of the form

$$h_{\ell,m} = \frac{\alpha\rho_s}{\rho_s - \rho_w}\int_0^{\mathrm{CMB}} H_\ell \Delta T_{\ell,m} dr \qquad (3)$$

in which α is the coefficient of thermal expansion; ρ_s and ρ_w are the densities of the mantle and water, respectively; and the integral is taken along the radial direction r from the surface through the convecting region to the core-mantle boundary (CMB). The topography kernel H_ℓ can be calculated from the equations of continuity and motion given a set of boundary conditions, a viscosity model, and a constitutive relation between stress and strain. Similarly, the kernel for the geopotential G_ℓ relates the thermal anomalies to the geoid $N_{\ell,m}$ via

$$N_{\ell,m} = \frac{3\alpha\rho_s}{\rho_{av}(2\ell + 1)}\int_0^{\mathrm{CMB}} G_\ell \Delta T_{\ell,m} dr \qquad (4)$$

in which ρ_{av} is the average density of the earth. With these definitions, the theoretical geoid/topography admittance Z_ℓ is

$$Z_\ell(r) = \frac{3(\rho_s - \rho_w)}{\rho_{av}(2\ell + 1)} \frac{G_\ell(r)}{H_\ell(r)} \quad (5)$$

for a temperature spike at depth r (Fig. 9).

Several simple mantle viscosity models can be clearly rejected on the basis of even these meager admittance data. For example, no possible vertical distribution of temperature in the convecting mantle will allow a geoid low and a topographic high at any wavelength if the mantle has a uniform viscosity and is either chemically uniform (Fig. 9A) or chemically layered (Fig. 9B). The only way we were successful in producing negative admittances was to include a low-viscosity zone at the base of the lithosphere (Fig. 9, C and D). If hot material is near the base of or just below such a low-viscosity layer, this weak layer ineffectively transmits the vertical normal stress from the upward flow induced by the buoyant mass to the surface, producing little surface uplift. Rather, most of the compensation for the low-density rock lies beneath it at the CMB or any other interior density discontinuities because of more effective transmittal of stress through the deeper high-viscosity region. The contributions to the geoid anomaly include a relatively minor mass excess at the surface from the small amount of dynamic surface topography, a larger mass deficit from the hot convecting material, and another mass excess at the CMB, whose geoid signal at wavelengths less than 3000 km is severely attenuated at the surface. The sum of all of these mass anomalies is approximately zero to bring about isostasy, but the geoid low from the hot material dominates the overall signal because it is larger than the mass excess from surface uplift and much shallower than the mass excess at the CMB.

Our estimate of the thickness of the low-viscosity zone beneath the Superswell is controlled by the change in sign of the observed admittance. It must be several hundred kilometers thick in order to produce negative geoid/topography ratios at wavelengths of several thousand kilometers, but it cannot extend throughout the entire upper mantle without producing negative ratios at all wavelengths. There is some trade-off between thickness of the low-viscosity zone and the magnitude of the reduction in viscosity (Fig. 9, C and D), but in general the low-viscosity zone must be several hundred kilometers thick (that is, extend to the transition zone) and involve a reduction in viscosity by a factor of 50 to 100 from the value characteristic of the lower mantle. For the preferred solutions, the magnitudes of the kernels below the lithosphere for topography are small at $\ell = 16$ but large at $\ell = 8$. Exactly the reverse is true for the geoid. This pattern may account for why a geoid high correlated with the longest wavelength of the depth anomaly as determined by the admittance is not visually apparent, whereas the geoid low across the swell from north to south is so prominent.

In order for this viscosity model to reproduce the observations from the Superswell, the thermal structure within the convecting region must concentrate its high temperatures near the base of this low-viscosity zone. The two-dimensional, Cartesian convection calculations of Robinson (*23*) do indeed show that a narrow upwelling plume tends to spread out when it reaches the low-viscosity zone, producing the largest lateral variations in temperature near the base of the low-viscosity layer. This calculation needs to be repeated for the spherical geometry and scales appropriate for the Superswell. One model of *P*-wave tomography (*24*) shows hot temperatures anomalies (+40°C) at depths of 300 to 600 km directly beneath the Superswell and little structure at greater depth. If we assume that this temperature excess of 40°C is uniformly distributed throughout a layer 300 km thick between 300 and 600 km, Eqs. 3 and 4 predict a dynamic depth anomaly of about 200 m and a geoid anomaly of −5 m, in rough agreement with the data. This simple model in no way represents all of the complexity in the geoid and depth anomalies in this area. For example, we do not attempt to model the geoid high over the East Pacific Rise along the eastern edge of the region, where the thickness of the high-viscosity lid thins to zero and there may be deeper lateral variations in viscosity as well.

Our conclusion from the Love-wave modeling that temperature anomalies below 125 km do not contribute to the slow surface wave velocities across the Superswell is also confirmed by the geoid analysis; the thermal anomalies in the convecting mantle responsible for the dynamic topography and geoid anomalies are both small in magnitude compared to the +300°C anomalies in the lithosphere and are located at depths where the Love-wave kernels are small. Thermal anomalies between 125 and 300 km must also be present in any steady-state system, but the existing observations give little information on their magnitude. The *P*-wave ray paths did not sample this depth region, the geoid kernels (Fig. 9, C and D) change sign, which cancels out any effect from these depths, and any contribution to the Love-wave and depth anomalies are overshadowed by the lithospheric signal.

Discussion

Our conclusion that a low-viscosity zone underlies the lithosphere in French Polynesia should come as no surprise. Such a layer must be widespread beneath the oceanic lithosphere, otherwise there

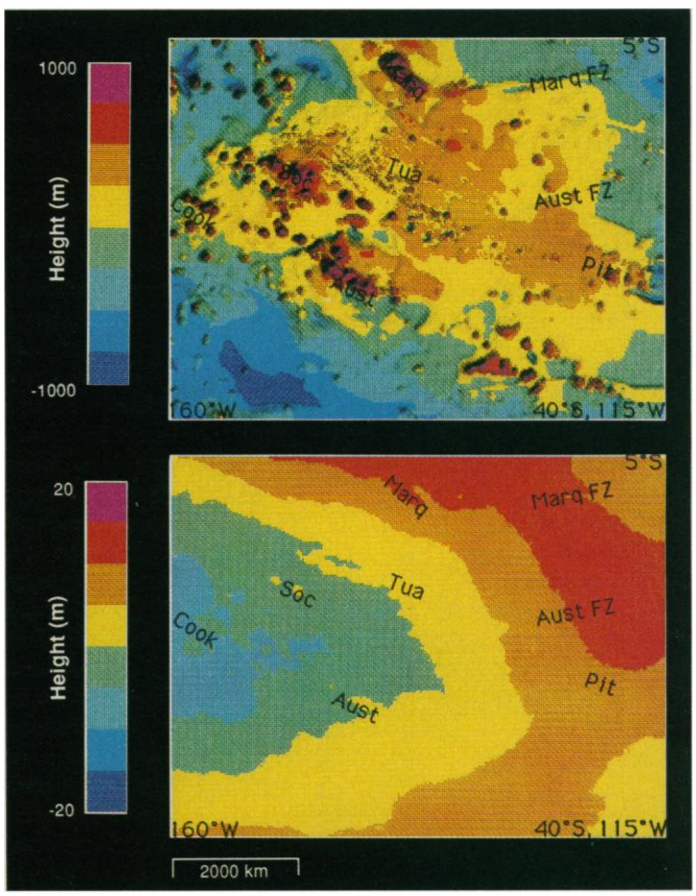

Fig. 7. Depth (**top**) and geoid (**bottom**) anomalies over the Superswell as in Fig. 2 but referenced to a 75-km-thick thermal plate and with the bathymetric and geoid signatures of the Society, Austral, and Pitcairn swells and the Tuamotu Plateau removed.

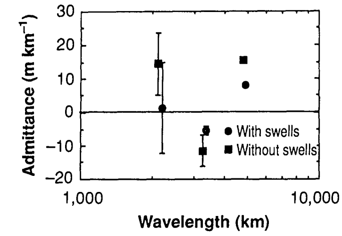

Fig. 8. Admittance calculated from depth and geoid anomalies over the Superswell (*30*). The dots are the admittance values for depth and geoid anomalies referenced to a 75-km-thick plate, but without the swells removed from the data. The squares are the admittance values from the data in Fig. 7.

would be a much stronger correlation between depth of the sea floor and long-wavelength geoid anomalies that would preclude observing the depth increase caused by cooling of the lithosphere. The presence of a low-viscosity zone in the asthenosphere is also predicted by the temperature and pressure dependence of viscosity for upper mantle materials from laboratory experiments (*23*), but the large reduction in viscosity that we observe here may require the presence of partial melt or a high volatile content, in addition to elevated temperatures. We doubt that partial melting can also account for why the effective $\partial\beta/\partial T$ determined from modeling the age dependence of Love-wave phase velocity on normal oceanic lithosphere is nearly twice the value derived from laboratory calibrations under conditions of constant pressure (*25*), because the same value for $\partial\beta/\partial T$ fits the data for normal 10- to 50-million-year-old lithosphere, where melt is more likely to occur, as for 90- to 125-million-year-old lithosphere, where partial-melt zones are less likely (Fig. 3).

On the basis of this analysis, the thinned lithosphere proposed by McNutt and Fischer (*2*) is not the primary feature of the Superswell; rather, it is the consequence of enhanced heat flux from the convecting mantle and low viscosity beneath the plate, both of which prevent the growth of a stable lithospheric thermal boundary layer to thicknesses greater than 75 km. The shallow depth to the base of the plate might be maintained by small-scale convective instabilities in the low-viscosity zone, such as have been proposed for this area as a result of the observation of short-wavelength gravity undulations aligned in the direction of Pacific plate motion (*26*). By attributing the fundamental origin of the Superswell to unusual mantle as opposed to lithospheric properties, this model also provides a natural link to the geochemical signature of the hot spot lavas and the rapid plate motion. For example, if the radiogenic enrichment of the hot spots is also characteristic of the mantle beneath French Polynesia, decay of long-lived radioactive isotopes could provide the heat source for the Superswell (*9*). Furthermore, because motion of the Pacific plate is the consequence of the gravitational pull of dense lithospheric slabs subducting along the western Pacific trenches, the low viscosity in the upper mantle beneath the Superswell would facilitate rapid plate motion with respect to the mantle by reducing the asthenospheric drag on the base of the lithosphere.

Although it is tempting to attribute the Superswell to the combined effects of many hot spots fortuitously located beneath French Polynesia, the concentration of hot spot volcanism here appears to be a consequence, rather than a cause, of the Superswell. The thinned lithosphere has been more easily penetrated by numerous, but relatively weak, thermal plumes (*10, 22*) that were incapable of producing midplate volcanoes on normal lithosphere immediately to the north of the Superswell as it passed over these same hot spots (*2*). Before their Tertiary activity on the Superswell, the last time that the hot spots of French Polynesia produced major volcanic chains was in the Cretaceous (100 Ma), when an earlier superswell existed over this same region of the mantle and was similarly associated with radiogenically enriched lavas and rapid plate velocity (*8, 9*).

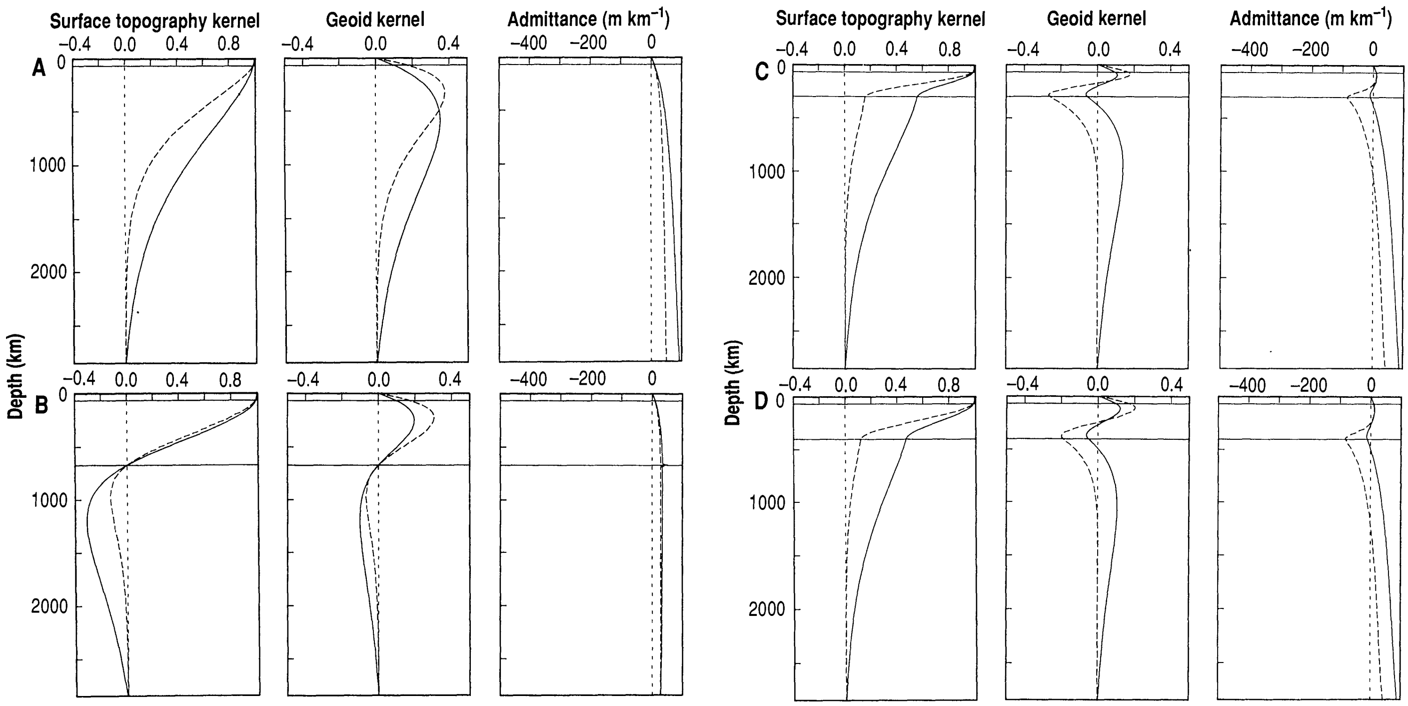

Fig. 9. Topography, geoid, and admittance kernels for $\ell = 8$ (wavelength of 4700 km) (——) and $\ell = 16$ (wavelength of 2400 km) (------) assuming various viscosity models for an incompressible, self-gravitating, Newtonian mantle with free slip at the surface and the CMB. The convecting region is overlain by a high-viscosity layer 70 km thick (*31*). We calculated kernels using a method similar to that of Richards and Hager (*32*) except that the solution was directly integrated across the layers instead of being obtained via propagator matrices. (**A**) Mantle assumed to be of uniform viscosity and chemically homogeneous. (**B**) Uniform viscosity mantle, but with a chemical discontinuity at a depth of 670 km that prevents flow across that boundary. (**C**) Plate underlain by a zone extending to a depth of 300 km with 1/100th the viscosity of the underlying mantle. (**D**) Plate underlain by a zone extending to a depth of 400 km with 1/50th the viscosity of the underlying mantle.

REFERENCES AND NOTES

1. B. E. Parsons and J. G. Sclater, *J. Geophys. Res.* **82**, 803 (1977).
2. M. K. McNutt and K. M. Fischer, in *Seamounts, Islands, and Atolls*, B. H. Keating, P. Fryer, R. Batiza, G. W. Boehlert, Eds. (Geophysical Monograph 43, American Geophysical Union, Washington, DC, 1987), pp. 25–34.
3. C. E. Nishimura and D. W. Forsyth, *Geophys. J. R. Astron. Soc.* **81**, 389 (1985).
4. M. K. McNutt and H. W. Menard, *J. Geophys. Res.* **83**, 1206 (1978).
5. S. Calmant and A. Cazenave, *Nature* **328**, 236 (1987).
6. S. R. Hart, *ibid.* **309**, 753 (1984).
7. J. B. Minster and T. X. Jordan, *J. Geophys. Res.* **83**, 5331 (1978).
8. M. K. McNutt *et al.*, *Geophys. Res. Lett.*, in press.
9. W. H. F. Smith, H. Staudigel, A. B. Watts, M. S. Pringle, *J. Geophys. Res.* **94**, 10501 (1989).
10. N. H. Sleep, *ibid.*, in press.
11. We neglect the contribution to the phase velocity anomalies from $\partial C_n/\partial \rho \cdot \partial \rho/\partial T$ because it is much smaller in magnitude and oscillates about zero through the upper few hundred kilometers. See W. L. Rodi, P. Glover, T. M. C. Li, S. S. Alexander, *Bull. Seismol. Soc. Am.* **65**, 1105 (1975).
12. Although $\partial C_n/\partial \beta$ appears to be dimensionless, it has units of 1/length. See K. Aki and P. G. Richards, *Quantitative Seismology* (Freeman, San Francisco, 1980).
13. K. M. Fischer, thesis, Massachusetts Institute of Technology, Cambridge (1988).
14. D. L. Anderson, *Phys. Earth Planet. Inter.* **45**, 307 (1987).
15. G. M. Purdy, *J. Geophys. Res.* **92**, 9351 (1987).
16. A simple thickening of the low-velocity crust cannot account for the anomalies. Even if the crust in the south-central Pacific were thick enough to completely account for its shallow depth, the calculated amplitude of velocity anomalies for surface waves propagating across it would be too small by a factor of 8 for 40-s waves and would decrease too slowly with increasing period as compared to the observed anomalies.
17. J. Talandier and E. A. Okal, *Geophys. J. R. Astron. Soc.* **88**, 499 (1987).
18. M. K. McNutt and L. Shure, *J. Geophys. Res.* **91**, 13915 (1986).
19. A. Sheehan and M. McNutt, *Earth Planet. Sci. Lett.* **93**, 377 (1989).
20. The model assumes that the topography and geoid arise from lithospheric heating rather than dynamic flow. This choice is immaterial for adequately predicting the swell signatures but would affect the interpretation of the physical parameters in the model. See E. M. Robinson, B. E. Parsons, S. F. Daly, *Earth Planet. Sci. Lett.* **82**, 335 (1987).
21. M. K. McNutt, in *Seamounts, Islands, and Atolls*, B. H. Keating, P. Fryer, R. Batiza, G. W. Boehlert, Eds. (Geophysical Monograph 43, American Geophysical Union, Washington, DC, 1987), pp. 123–132.
22. C. W. Devey *et al.*, *J. Geophys. Res.*, in press.
23. E. M. Robinson, thesis, Massachusetts Institute of Technology, Cambridge (1987).
24. B. H. Hager and R. W. Clayton, in *Mantle Convection*, W. R. Peltier, Ed. (Gordon and Breach, New York, 1989), pp. 657–763.
25. M. Kumozawa and O. L. Anderson, *J. Geophys. Res.* **74**, 5961 (1969).
26. W. F. Haxby and J. K. Weissel, *ibid.* **91**, 3507 (1986).
27. Digital bathymetric database 5, J. R. Heirtzler, Ed. (National Geophysical Data Center, Boulder, CO, 1985).
28. J. G. Marsh *et al.*, *J. Geophys. Res.* **91**, 3501 (1986).
29. A. M. Dziewonski *et al.*, *Phys. Earth Planet. Inter.* **10**, 12 (1975).
30. The admittance is defined as $\langle N \cdot H^* \rangle / \langle H \cdot H^* \rangle$, where N and H are the Fourier transforms of geoid and depth, respectively, the asterisk denotes complex conjugation, and brackets indicate azimuthal averaging in wave number bands centered on a given frequency. The error in the admittance z is computed from $\{[\langle N{\cdot}N^* \rangle - 2z\langle N{\cdot}H^* \rangle + z^2\langle H{\cdot}H^* \rangle]/[(n-1)\langle H{\cdot}H^* \rangle]\}^{1/2}$ in which n is the number of spectral ratios in the wave number band. There is no error estimate for the longest wavelength value in Fig. 8 because $n = 1$. For admittance estimates at wavelengths of 3300 km and 2200 km, n equals 8 and 12, respectively.
31. If we adopt a 70-km-thick high-viscosity layer, we err on the side of using a layer too thick to mimic the effect of a 75-km thermal plate because of entrainment of a boundary layer in the lower viscosity medium below. As the viscosity of the upper mantle decreases, the thickness of the boundary layer decreases.
32. M. A. Richards and B. H. Hager, *J. Geophys. Res.* **89**, 5987 (1984).

33. We thank C Nishimura, S. Solomon, and L. Gee for enlightening discussions on surface waves. This work was supported by National Science Foundation grant 8710222-OCE.

Radar Reflectivity of Titan

DUANE O. MUHLEMAN, ARIE W. GROSSMAN, BRYAN J. BUTLER, MARTIN A. SLADE

The present understanding of the atmosphere and surface conditions on Saturn's largest moon, Titan, including the stability of methane, and an application of thermodynamics leads to a strong prediction of liquid hydrocarbons in an ethane-methane mixture on the surface. Such a surface would have nearly unique microwave reflection properties due to the low dielectric constant. Attempts were made to obtain reflections at a wavelength of 3.5 centimeters by means of a 70-meter antenna in California as the transmitter and the Very Large Array in New Mexico as the receiving instrument. Statistically significant echoes were obtained that show Titan is not covered with a deep, global ocean of ethane, as previously thought. The experiment yielded radar cross sections normalized by the Titan disk of 0.38 ± 0.15, 0.78 ± 0.15, and 0.25 ± 0.15 on three consecutive nights during which the sub-Earth longitude on Titan moved 50 degrees. The result for the combined data for the entire experiment is 0.35 ± 0.08. The cross sections are very high, most consistent with those of the Galilean satellites; no evidence of the putative liquid ethane was seen in the reflection data. A global ocean as shallow as about 200 meters would have exhibited reflectivities smaller by an order of magnitude, and below the detection limit of the experiment. The measured emissivity at similar wavelengths of about 0.9 is somewhat inconsistent with the high reflectivity.

TITAN IS ONE OF THE MOST INTERESTING OBJECTS IN OUR solar system. Although it was discovered in 1655, little was known about it previous to the Voyager 1 flyby in 1980. This flyby supplied us with extensive atmospheric information, including the temperature-pressure profile (*1*), and composition (*2*). The atmosphere consists mainly of N_2 with traces of hydrocarbons and nitriles including ethane, methane, acetylene, and HCN. Methane and CO have also been detected in Earth-based observations (*3*). However, because of its extensive hazy atmosphere, little was learned about the surface of Titan except that the temperature is 94 K, which varies only by a few kelvin from equator to pole (*1, 4*), and the atmospheric pressure is 1.5 bars. Even though the surface data are sparse, they can be combined with thermodynamical data on the chemical species to make important predictions about the state of

D. O. Muhleman, A. W. Grossman, and B. J. Butler are in the Division of Geological and Planetary Sciences, California Institute of Technology, Pasadena, CA 91125. M. A. Slade is at Jet Propulsion Laboratory, California Institute of Technology, Pasadena, CA 91109.